

Chern Insulators and Topological Flat-bands in Magic-angle Twisted Bilayer Graphene

Shuang Wu^{1†}, Zhenyuan Zhang^{1†}, K. Watanabe², T. Taniguchi², and Eva Y. Andrei^{1*}

¹Department of Physics and Astronomy, Rutgers University, New Jersey, 08854, USA

²National Institute for Materials Science, Namiki 1-1, Tsukuba, Ibaraki 305 0044, Japan

† These authors contributed equally to the work.

* Corresponding author. Email: andrei@physics.rutgers.edu

Magic-angle twisted bilayer graphene (MA-TBG) features intriguing quantum phase transitions between strongly correlated states with superconducting, ferromagnetic or nematic properties. Their emergence is triggered by enhanced electron-electron correlations when the flat bands in MA-TBG are partially filled. To date however, questions concerning the nature of these states and their connection to the putative non-trivial topology of the flat bands in MA-TBG, are largely unanswered. Here we report on magneto-transport and Hall density measurements that reveal a succession of doping-induced Lifshitz transitions where discontinuous changes in the Fermi surface topology are accompanied by van Hove singularity (VHS) peaks in the density of states (DOS) that facilitate the emergence of correlation-induced gaps and topologically non-trivial sub-bands. In the presence of a magnetic field the topology of the sub-bands at filling of 1, 2, 3 carriers per moiré cell is revealed through well quantized Hall plateaus signaling the appearance of Chern insulators with Chern numbers, $C = 3, 2, 1$, respectively. Surprisingly, for magnetic fields exceeding 5T we observe a new VHS at a filling of 3.5 electrons per moiré cell, suggesting the possibility of a topological sub-band at a fractional moiré filling.

The band structure of twisted bilayer graphene is strongly renormalized by the moiré superstructure that forms in the presence of a small twist angle between the crystal orientations of the two layers.¹⁻⁷ Close to the 'magic' twist-angle, $\theta \sim 1.1^\circ$, the low energy electronic structure of MA-TBG consists of two four-fold degenerate nearly-flat bands,^{3,8} that straddle the charge neutrality point (CNP) and are separated from higher energy bands by spectral gaps. Aligning the Fermi level with these flat bands facilitates interaction-induced instabilities leading to strongly correlated behavior^{6,7,9-13} and to the creation of flavor-polarized (spin/valley) moiré sub-bands with non-trivial topology^{14,15}. These sub-bands can be mapped onto an eightfold degenerate manifold of zeroth pseudo Landau levels (pLL) generated by Dirac fermions that are coupled with opposite sign pseudo-magnetic fields in each of the two flat bands¹⁴. The non-trivial topology of the pLL sub-bands is characterized by opposite Chern numbers $C = +1$ or -1 , for opposite sublattice polarizations A or B in each mini-Brillouin zone valley, K_s and K_s' , as illustrated in Extended Data Figure 1. In the absence of broken $C_{2z} \mathcal{T}$ symmetry ($C_{2z} = 180^\circ$ in plane rotation and \mathcal{T} = time reversal), the bands are degenerate and their non-trivial topology is hidden. Lifting this degeneracy, by explicitly breaking time reversal or sublattice symmetry, is expected to reveal the topological nature of these bands and its role in shaping the correlated phases in this system, but thus far experimental evidence is limited. Here we uncover the interplay between the emergence of correlated insulating phases at integer fillings and the non-trivial topology of the flat bands, as revealed by the observation of their finite Chern numbers in the presence of an external magnetic field.

Full and half-full Landau fans at integer moiré fillings

We focus on transport measurements on a MA-TBG sample prepared by the "tear and stack" technique¹⁶ (Methods) with twist angle $\theta \approx 1.17^\circ \pm 0.02$, shown in Fig. 1a. The Hall and longitudinal resistance, R_{xy} and R_{xx} , were obtained with a 4-terminal lead configuration. At low temperatures $R_{xx}(n)$ develops strong peaks at integer moiré cell fillings, $|n/n_0| = 0, 2, 3$, and diverges at the band edges, $|n/n_0| = 4$, (Fig. 1b) consistent with previous results.⁶ Here n is the gate controlled carrier density, n/n_0 is the number of carriers per moiré cell (moiré filling factor),

$n_0 = 2/\sqrt{3}/(\theta/a)^2$ corresponds to one carrier per moiré cell, $a=0.246\text{nm}$ is graphene's lattice constant, and θ is the twist angle in radians. Close to $n/n_0 = -2$ (2 holes per moiré cell) we observe the signature of superconductivity with a maximum critical temperature of $T_c \sim 3.5\text{K}$ (Extended Data Figure 2), consistent with earlier reports in similar devices.^{7,9} Since superconductivity is not the focus of this work all measurements were carried out at magnetic fields or driving currents where superconductivity is quenched.

The density and magnetic field (B) dependence of R_{xx} , shown in Fig. 1c, features Shubnikov de Haas minima (Extended Data Figure 3) resulting in Landau fans whose pleats (trajectories) can be parameterized according to $n/n_0(s, \nu) = s + \nu (\phi/\phi_0)$ where $s, \nu \in \mathbb{Z}$ and $s = 0$ or $s \cdot \nu < 0$. Here ϕ is the magnetic flux per moiré unit cell, $\phi_0 = h/e$ is the magnetic flux quantum, h is Planck's constant, ν is the flux filling factor which measures the number of carriers per flux line, and s is the moiré filling factor (branch index) which corresponds to the number of carriers per moiré cell in zero field. Trajectories emanating from the CNP, $s = 0$, form a bilateral (full) Landau fan, with $\nu = \pm 1, \pm 2, \pm 3, \pm 4, \pm 8, \pm 12 \dots$, which are characteristic of Landau levels in a system where both electron and hole carriers contribute to the fan. Unlike the full-Landau fans observed in the $s = 0$ branch, the trajectories on the $s \neq 0$ branches form unilateral (half) Landau fans that slope away from the CNP, corresponding to $s \cdot \nu > 0$. These trajectories are labeled by a partial Diophantine equation which resembles the non-interacting Hofstadter butterfly spectrum, but the underlying physics of the two phenomena is different. The half-fans observed here, are a direct consequence of correlation-induced spectral gaps which emerge on any $s \neq 0$ branch only after the doping level has reached the corresponding integer moiré filling, while they are absent on the low filling side of the branch. This is in contrast to the bilateral Hofstadter butterflies which reflect rigid Bloch bands where the gaps are independent of filling.¹⁷

From R_{xx} and R_{xy} , we obtain the corresponding conductivities, $\sigma_{xy} = R_{xy}/(R_{xy}^2 + (w/l)^2 R_{xx}^2)$ and $\sigma_{xx} = (w/l)R_{xx}/(R_{xy}^2 + (w/l)^2 R_{xx}^2)$, where $w/l = 0.625$ is the sample aspect ratio (Fig. 1d and Extended Data Figure 4). To avoid artifacts associated with lead asymmetry, the data is presented in terms of symmetrized resistances: $\bar{R}_{xx}(B) = (R_{xx}(n, B) + R_{xx}(n, -B))/2$ and $\bar{R}_{xy}(B) =$

$(R_{xy}(B) - R_{xy}(-B))/2$, henceforth labeled R_{xx} and R_{xy} respectively. The high quality of this sample is reflected in the appearance of well-quantized σ_{xy} plateaus and σ_{xx} minima on the $s = 0$ branch. At $B \sim 1.5\text{T}$, the $s = 0$ bilateral fan develops a quantized Hall plateau sequence $\sigma_{xy} = \nu e^2/h$, initially with $\nu = \pm 4, \pm 8$ reflecting the 4-fold degeneracy of the bands (Extended Data Figure 3a). At higher fields, $B > 5\text{T}$, the addition of all odd-index plateaus to the sequence $\nu = 0, 1, \pm 2, \pm 3, \pm 4$ reflects the formation of quantum Hall states with fully lifted spin and valley degeneracies (Fig. 1d). The well-defined integer quantum Hall plateaus, are testimony to the high quality of the sample which is essential for probing the Fermi surface topology.

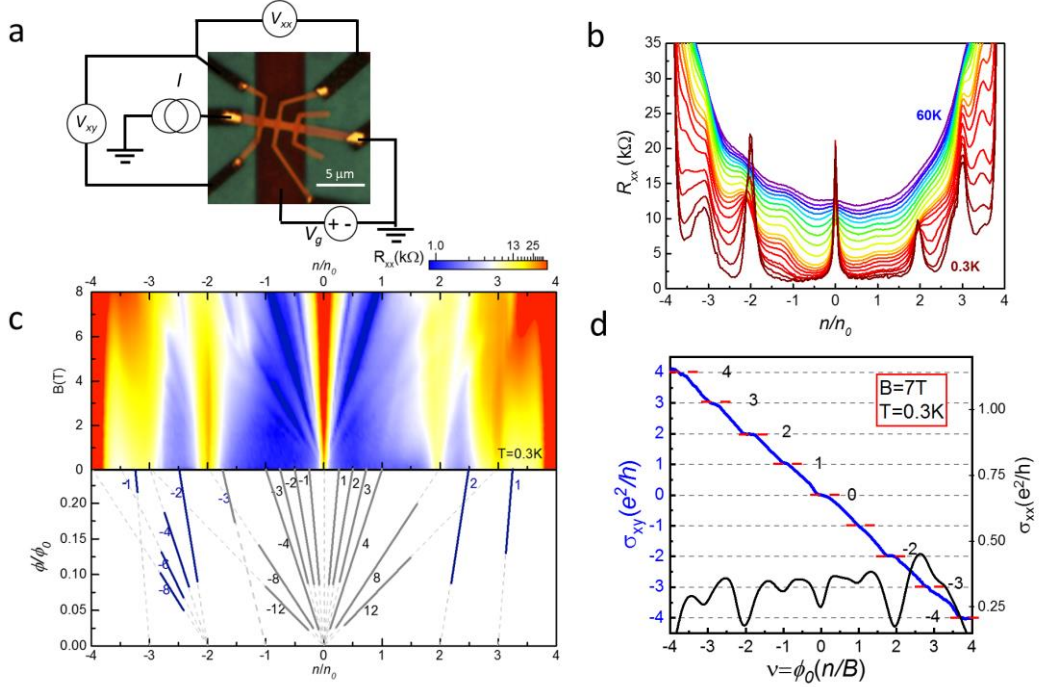


FIG. 1. Correlated states, Landau fans and quantum Hall plateaus

(a) Optical micrograph of the device with schematic of multi-terminal measurements. **(b)** Temperature dependence of the longitudinal resistance, R_{xx} , versus moiré filling (n/n_0) at $B = 0\text{T}$ from 60K down to 0.3K (driving current 100nA). **(c)** Top: $R_{xx}(B, n/n_0)$. Bottom: Landau fans are parameterized by the pleat and branch index $\nu, s \in \mathbb{Z}$. Gray trace the $s = 0$ full-Landau fan, and blue lines trace the $s \neq 0$ half-Landau fans attributed to Chern insulators. **(d)** σ_{xy} and σ_{xx} as a function of Landau level filling for $s = 0$ at $B = 7\text{T}$, $T = 0.3\text{K}$ shows a well-defined quantum Hall plateau sequence $\sigma_{xy} = \nu e^2/h$ (dashed red lines) and minima of σ_{xx} at $\nu = 0, 1, \pm 2, \pm 3, \pm 4$.

Van Hove singularities and band reconstruction probed by the Hall density

Electron-electron interactions leading to complex quantum phases, can be significantly enhanced by DOS peaks, such as van Hove singularities (VHS), where the Fermi surface area and its topology changes. Experimentally, such Fermi surface topology changes, known as Lifshitz transitions^{18,19}, can be inferred from the Hall density, $n_H = -B/(eR_{xy})$, (e is the elementary charge). For a clean 2D system, in the low temperature limit, with closed Fermi pockets, $n_H = DA_{FS} = n$, (D is the degeneracy) provides access to the net area enclosed by the Fermi surface, A_{FS} . Far from Lifshitz transitions, n_H measures the free carrier density which determines transport properties²⁰. Upon approaching a VHS, n_H diverges logarithmically with opposite signs on the low and high density sides of the VHS. However, when the bands become malleable as often happens when the Fermi level approaches a VHS, this is no longer the case. If for example a gap opens upon crossing the VHS, n_H resets to zero in the newly created empty band. Beyond this point, n_H still increases linearly with n , but with an offset: $n_H = n - n_c$, where n_c marks the density at which the gap opened. Spectral gaps that emerge in the absence of VHS, for example by magnetically induced enhanced interactions, can generate a similar offset in n_H , but without being preceded by a logarithmic divergence. Thus, the evolution of n_H with doping provides access to the Fermi surface reconstruction and to the emergence of broken symmetry states as the chemical potential is swept across the band²¹.

We next discuss measurements of n_H that revealed the emergence of gaps at integer fillings and the appearance of sub-bands with non-trivial topology. The doping dependence of $R_{xy}(n)$ from which we extract $n_H(n)$ at $B = 0.8\text{T}$, $T = 0.3\text{K}$, is shown in Fig. 2a,b. For $0 \leq |n/n_0| < 2$ we find that $n_H \approx n$ (Fig. 2b), indicating that the Fermi surface consists of closed pockets. Upon approaching $|n/n_0| = 2$ from the low-density side, the strong deviation from $n_H \approx n$ fits the expression describing the Lifshitz transition at a VHS in the low-field limit (Extended Data Figure 5)²¹, $n_H \approx \alpha + \beta(n - n_c)\ln|(n - n_c)/n_0|$, α, β are constants, and $n_c = \pm 2n_0$. According to theoretical models²² the non-interacting, rigid, band structure of MA-TBG contains two VHS that separate a two-pocket Fermi surface centered on the K_s, K_s' valleys at $|n/n_0| < 2$ from a higher energy single pocket Fermi-surface centered on the Γ point at $|n/n_0| > 2$ (inset Fig. 2b

and Extended Data Figure 1b)²². Experimentally however, the logarithmic divergence of n_H expected to appear on the high-density side of n_c for a VHS in a rigid band structure, is not observed here. Instead, upon crossing the VHS, n_H resets to zero and subsequently increases linearly, $n_H = n \pm 2n_0$, in both the conduction (−) and valence (+) bands, signaling a correlation-induced reconstruction of the band. The fact that the value of n_H resets to zero shows that doping the system across $|n/n_0| = 2$, not only changes the Fermi surface topology but also reconstructs the band by creating a correlation-induced gap with broken flavor symmetry. As a result, the initially 4-fold flavor degenerate band breaks up into two 2-fold flavor degenerate sub-bands, one full and the other empty, which can each accommodate 2 carriers per moiré cell (Extended Data Figure 1c). Doping the sample beyond this level starts filling the higher energy sub-band which again consists of closed Fermi pockets. This band reconstruction also explains the appearance of the Landau fan on the high-density side of the $s = \pm 2$ branches and its absence on the low-density sides.

As doping continues to increase towards $|n/n_0| = 3$, the Hall density deviates from $n_H = n \pm 2n_0$, and it again displays the logarithmic divergence characteristic of a VHS (solid line in Fig. 2b). The fact that at low fields this divergence appears on both sides, of $|n_c/n_0| \sim 3$, together with the absence of a Landau fan, indicates that no gap opens when the Fermi level crosses this VHS. The approach to this VHS is accompanied by the appearance of strong R_{xx} peaks at $|n/n_0| \sim 3$ (Fig. 2a) which is consistent with the singular DOS and concomitant suppression of the Fermi velocity expected at a VHS.²³⁻²⁵ The logarithmic divergence of n_H and its appearance in tandem with the peak in R_{xx} , provide a unique fingerprint that enables us to identify the VHS in this system.

With increasing magnetic field this picture changes substantially, as illustrated in Fig. 2c where we plot the field dependence of R_{xy} measured at a constant density, e.g. $n/n_0 = 3.3$. At low fields, R_{xy} grows linearly with field, with a slope corresponding to $n_H = -1.5n_0$, indicating hole carriers. This value differs from that expected for a closed Fermi surface at this filling, $n_H = n - 4n_0 = 0.7n_0$, because of the proximity to the VHS at $n/n_0 = 3$. Beyond $B \sim 3$ T, a sharp change in the slope of R_{xy} , together with a sign change in n_H signals the formation of a correlation induced gap and the appearance of electron-like charge carriers near

the bottom of the newly created sub-band. In Fig. 2d, we compare the Hall density n_H at low and high fields in this filling range. At $n/n_0 = 3.3$, marked by the dashed line, the transition from the low field density dependence, $n_H = n - 4n_0$ to that at high field, $n_H = n - 3n_0$ after the gap opens is clearly resolved. Surprisingly, concomitant with the opening of the gap, we observe a logarithmically divergent n_H on both sides of $n/n_0 \sim 3.5$ which signals the appearance of a new VHS, seen in Fig. 2d (also Extended Data Figure 6). The pronounced R_{xx} peak observed at this filling (Fig 4c inset and Extended Data Figure 11), is again consistent with the singular DOS and simultaneous suppression of the Fermi velocity at a VHS.

As doping approaches the band edges, $|n/n_0| = 4$, (Figs. 2b, 2d), we observe $|n_H| = 4n_0 - |n|$ at all fields consistent with the theoretical prediction of a single hole (electron) pocket Fermi surface centered on the Γ -point in the completely full or empty band.²²

The evolution of the band structure observed here and its malleability in response to doping^{26,27} is schematically summarized in Fig. 2e. At low doping, close to the CNP, $n_H = n$, as expected for a rigid band. This rigidity is lost when the Fermi level approaches half filling, $|n/n_0| = 2$, where the large DOS of the VHS facilitates the emergence of a correlation-induced gapped state with broken flavor symmetry. This gap defines a new sub-band bracketed between $|n/n_0| = 2$ and $|n/n_0| = 4$ with a new VHS forming at its center, at $|n/n_0| \sim 3$, which in its turn gives rise at higher fields to a new gap and a sub-band bracketed between $|n/n_0| = 3$ and $|n/n_0| = 4$. In the case of the $s = -1$ branch no VHS is available to enhance e - e interactions and facilitate the emergence of a gap. As a result, the gap on this branch is purely field-induced and appears only above 6T as shown in Fig. 2f by the slope change of the Hall density from $n_H = n$ to $n_H = n + n_0$.

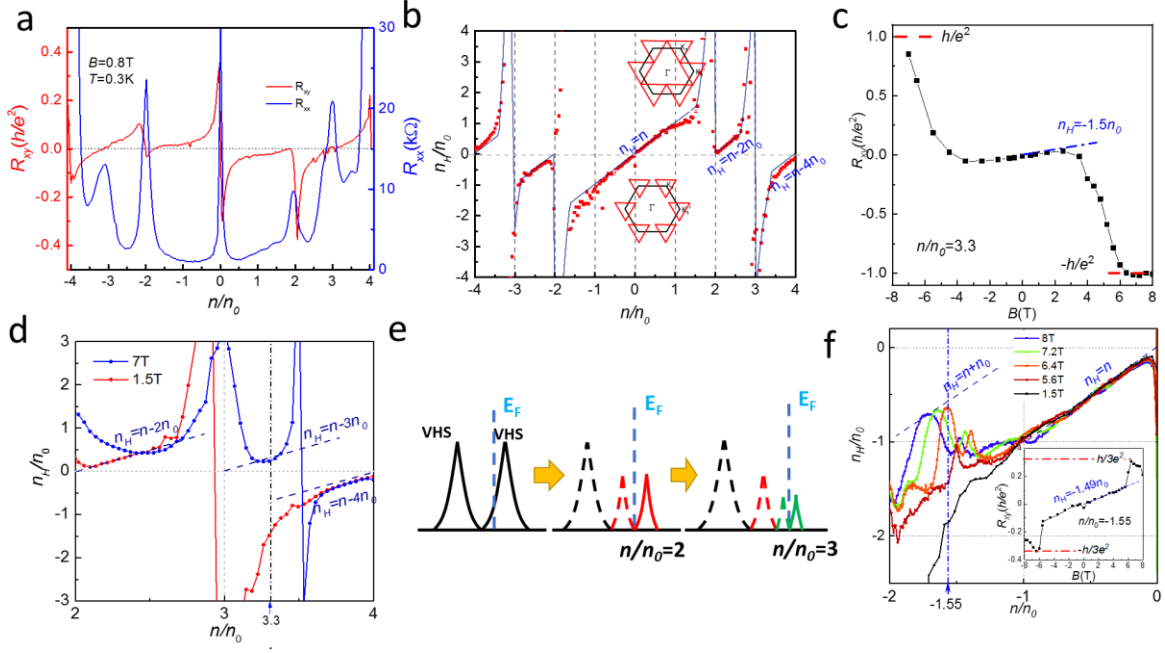


FIG. 2. Van Hove singularities, Fermi surface topology and correlation-induced sub-bands **(a)** Doping dependence of longitudinal and Hall resistance (R_{xx} and R_{xy}) at $B = 0.8\text{T}$, $T = 0.3\text{K}$. **(b)** Doping dependence of Hall density $n_H = -(1/e)(dR_{xy}/dB)^{-1}$ at $T = 0.3\text{K}$ (symbols) and fits (solid lines) to the logarithmic divergence characteristic of VHS near $|n/n_0| = 2, 3$. Inset, schematic evolution of the Fermi surface (red triangles) with doping. The separate pockets centered on K_s at low doping (bottom) merge near the VHS (top) at $|n/n_0| \sim 2$. **(c)** $R_{xy}(B)$ at $n/n_0 = 3.3$ at $T = 0.3\text{K}$. The low field slope of $R_{xy}(B)$ (blue dashed line) abruptly changes sign at $\sim 3.5\text{T}$ indicating a new sub-band. **(d)** Doping dependence of reduced Hall density, n_H/n_0 , near $n/n_0 = 3$ at $B = 7.0\text{T}$ and 1.5T for $T = 0.3\text{K}$. Arrow marks the density of the data in panel (b). Slopes corresponding to the density dependence in each branch are marked by dashed lines. The divergent Hall density near $n/n_0 = 3.5$ for $B > 5.0\text{T}$ signals a new VHS. **(e)** Evolution of DOS with Fermi energy shows that crossing a VHS produces a gap and a new sub-band with a VHS at its center. **(f)** Evolution of n_H/n_0 near $n/n_0 = -1$ at $T = 0.3\text{K}$. The slope change from $n_H = n$ at $B = 1.5\text{T}$ to $n_H = n + n_0$ for $B > 5.6\text{T}$ reveals a new sub-band associated with a magnetically induced correlation gap on the $s = -1$ branch. Inset: $R_{xy}(B)$ at $n/n_0 = -1.55$ and $T = 0.3\text{K}$. The low-field slope of $R_{xy}(B)$ (blue dashed line) corresponding to n_H , abruptly changes at $\sim 6\text{T}$ indicating a magnetically induced gap on the $s = -1$ branch.

Observation of field-induced Chern insulators

We next discuss the non-trivial topology of the sub-bands, as revealed by the Chern number obtained from the quantized Hall resistance. The contour maps of $R_{xy}(n, B)$ shown in Figs 3a,b and of $d^2 R_{xx}/dn^2$, shown in Extended Data Figure 7 reveal half-Landau fans on the $s = 3, \pm 2, -1$ branches. These fans consist each of a single pronounced pleat corresponding to the $\nu = 1, \pm 2, -3$ trajectories that extrapolate at zero field to integer moiré fillings, $n/n_0 = 3, \pm 2, -1$, respectively. The pleats on the $s = \pm 2$ branches persists down to the lowest fields, while the others appear in higher fields, above $B = 4\text{T}$ and $B = 6\text{T}$ for the $s = 3, -1$ branches respectively. With increasing field the Hall resistance on these pleats increases steadily and ultimately reaches the quantized value, $R_{xy} = \frac{1}{C} (h/e^2)$, where the Chern numbers $C = -1, \mp 2, 3$ characterize the sub-bands corresponding to the $s = 3, \pm 2, -1$ branches respectively, (Figs. 3c,d). A similar behavior is observed on the $s = -3$ branch (Extended Data Figure 8).

These results can be understood within the theoretical model describing the flat bands in MA-TBG as zeroth order eightfold degenerate (including physical spin) pseudo LLs¹⁴, corresponding to eight topological sub-bands. The sub-bands in each valley are labeled by three quantum numbers: the Chern number, $C = \pm 1$, which also corresponds to the sign of the pseudo-magnetic field, sublattice index A or B , and spin $\sigma = \uparrow, \downarrow$. From symmetry considerations only four states are possible in each valley, so that if states $|+, A, \sigma\rangle$ and $|-, B, \sigma\rangle$ are in the K valley then states $|-, A, \sigma\rangle$ and $|+, B, \sigma\rangle$ must be in the K' valley, as illustrated in Extended Data Figure 1c. Applying an external magnetic field produces an orbital magnetic Zeeman effect which splits the $C = +1$ and $C = -1$ Chern sub-bands, creating a single particle gap at the CNP. When the Fermi level is brought into one of these sub-bands, the exchange part of the Coulomb interactions further lifts their degeneracy resulting in the emergence of correlated insulating states at integer sub-band fillings, corresponding to integer moiré-cell fillings. Since each sub-band carries a finite Chern number, $C = \pm 1$, filling them would produce topological phases with nonzero total Chern number whose value depends on how they are filled. As we show below, all our results can be understood within this model, including the observation of correlation gaps at integer fillings, the formation of topologically non-trivial sub-bands, and the quantized Hall resistance.

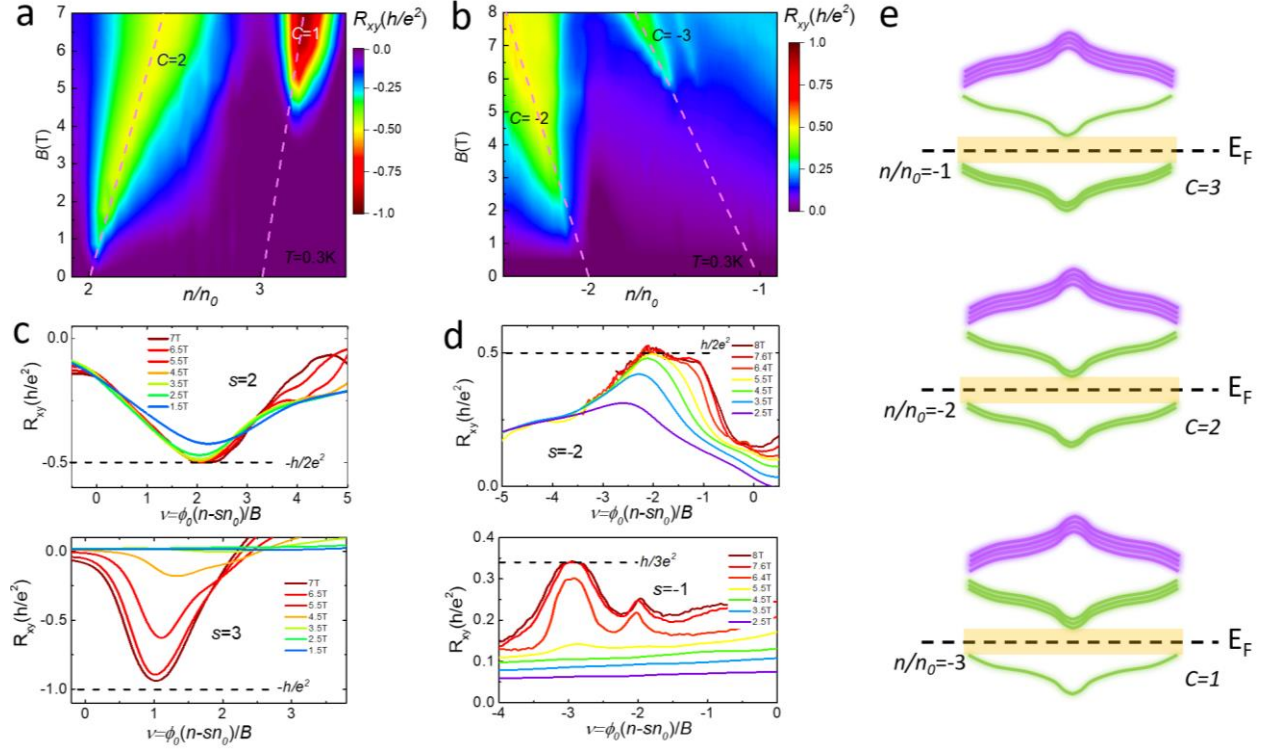


FIG. 3 Chern insulators at integer fillings (a-b) Evolution of $R_{xy}(n/n_0)$ with magnetic field in the conduction (a) and valence (b) bands shows the emergence of well-quantized Hall plateaus with Chern numbers $C = -2, -1, +2, +3$ on branches $s = 2, 3, -2, -1$ respectively. These Hall plateaus on each of these branches follow constant flux filling-factor trajectories with $\nu = -2, -1, +2, +3$ respectively. **(c-d)**, Field dependence of Hall resistance as a function of the flux filling factor, $\nu = \phi_0(n - sn_0)/B$, saturates to well-quantized Hall plateaus values, $R_{xy} = \frac{1}{C} \frac{h}{e^2}$ corresponding to Chern insulators with $C = -2, -1, +2, +3$ on branches $s = 2, 3, -2, -1$, respectively. **(e)** Schematic diagram depicts the appearance of the correlation gap and the formation of non-trivial topological sub-bands at integer fillings.

We first consider the states on the $s = \pm 3$ branches corresponding to filling a single electron or hole carrier per moiré cell. In high fields, the appearance of a doping induced correlation gap, splits off a low energy or high-energy sub-band for $s = -3$ or $+3$ respectively, as shown in Extended Data Figure 1c. Since only one out of the eight sub-bands is occupied (empty), the state must be ferromagnetic and carry a Chern number $C = \pm 1$, consistent with the observation of the quantized Hall resistance $R_{xy} = \mp h/e^2$ shown in Fig. 3c and Extended

Data Figure 8a. The evolution of the correlation gaps with in-plane magnetic field discussed below further supports this scenario. It is worth comparing with reports of a $C = 1$ Chern insulator observed at $n/n_0 = 3$, where the alignment with the hBN substrate, which breaks the C_2 symmetry by imposing a staggered sublattice potential^{14,28,29}, is responsible for opening the gap at very low magnetic fields (150mT). By contrast, in the data reported here there is no alignment with the hBN substrate, the C_2 symmetry is not explicitly broken, and the $n/n_0 = 3$ state is gapless at low fields. However once the gap opens, regardless of whether it is due to the staggered potential or the magnetic field, the topological nature of this sub-band becomes apparent as evidenced by the quantized Hall resistance.

For the $s = \pm 2$ branches, two out of the eight pLLs are occupied (empty). In the presence of the magnetic field, the four $C = +1$ ($C = -1$) Chern bands, which are lowest (highest) in energy due to the orbital Zeeman effect, will be occupied (emptied) first. Therefore, regardless of which of these four bands are occupied (empty), the resulting state will have a Chern number of $+2$ as observed experimentally (Figs. 3c,d). The final state could be either a valley polarized state or an inter-valley coherent state, depending on whether the two occupied bands are in the same valley (e.g. $|+1, A, \uparrow\rangle_K$ $|+1, A, \downarrow\rangle_K$) or in opposite valleys (e.g. $|+1, A, \uparrow\rangle_K$ $|+1, B, \downarrow\rangle_{K'}$ or $|+1, A, \uparrow\rangle_K$ $|+1, B, \uparrow\rangle_{K'}$) (Extended Data Figure 1c), however the magneto-transport measurements are unable to distinguish between these choices.

For $s = -1$, the three electrons in this state must occupy three of the four available lowest energy $C = +1$ Chern bands (Extended Data Figure 1c). This necessarily produces a ferromagnetic state with $C = +3$, consistent with the observed quantized Hall resistance, as seen in the bottom panel of Fig. 3d.

For the $s = 0$ branch, namely CNP, the four available lowest (highest) energy Chern bands, $C = +1$ ($C = -1$), are occupied producing a $C = +4$ ($C = -4$) state. However, the observation of the quantum Hall plateau sequence, $\nu = \pm 4, \pm 8$ already at the lowest fields, suggests that in the $s = 0$ branch 0 magnetically induced Landau level states prevail over the Chern insulator. This is in contrast to the $s \neq 0$ branches where only the quantum Hall plateau of the corresponding Chern insulator is observed. Hence we use different notations, C and ν , to distinguish between quantum Hall plateaus arising from the Chern insulator and Landau level scenarios respectively.

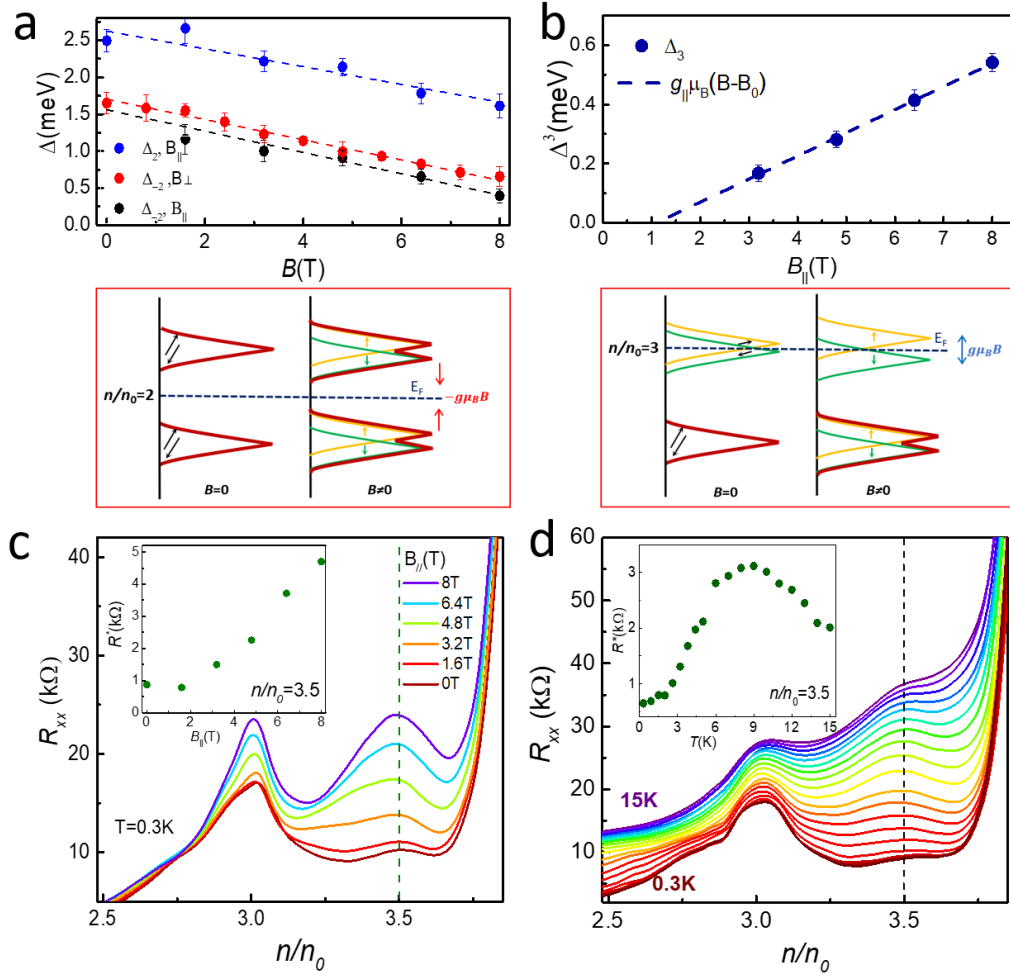


FIG. 4 Thermal activation gaps on the $s = 2, 3$ branches. **(a)** Top: in-plane and out-of-plane field dependence of the thermally activated gaps for states corresponding to $|s| = 2$ (symbols) as marked. Fits to the linear field dependence (dashed lines) indicate unpolarized insulating states as detailed in the text. Bottom: Diagram illustrating the evolution of the gap with magnetic field on the $|s| = 2$ branches. **(b)** Top: $B_{||}$ dependence of the gap on the $s = 3$ branch (symbols) and linear fit (dashed line) indicates a spin polarized insulating state. Bottom: Same as panel bottom of panel (a) for $s = 3$. **(c)** In-plane field dependence of R_{xy} (n/n_0) at $T = 0.3$ K. Inset: $B_{||}$ dependence of thermally activated portion of the longitudinal resistance, R^* , at $n/n_0 = 3.5$. **(d)** Temperature dependence of R_{xy} (n/n_0) in zero field. Inset: Temperature dependence of R^* , at $n/n_0 = 3.5$ shows a crossover from low temperature metallic, to high temperature insulating behavior at $T \sim 9$ K suggesting an entropically driven Pomeranchuk-like transition

Correlation gaps obtained from thermally activated transport

Having inferred the existence of the correlation-induced gaps from the doping dependence of n_H , we calculate their magnitude from the temperature dependence of the thermally activated part of the longitudinal resistance, R^* , obtained from $R_{xx}(T)$ after subtracting a linear in T background (Extended Data Figures 9,10).³⁰ Performing an Arrhenius analysis, $R^* \sim \exp(-\Delta_s/2k_B T)$, we obtained the thermally activated gaps, Δ_s , where s is the branch index and k_B is Boltzmann's constant. To gain insight into the nature of the Chern insulators we measure the field dependence of R^* for in plane ($B_{||}$) and out of plane (B_{\perp}) fields. As shown in Fig. 4a, Δ_2 and Δ_{-2} decrease linearly with both in-plane and out-of plane fields. This indicates that the $|n/n_0| = 2$ insulating states are not spin polarized (Fig 4a bottom panel), and can be described by either the valley polarized state $|+1, A, \uparrow\rangle_K | +1, A, \downarrow\rangle_K$ or the inter-valley coherent state $|+1, A, \uparrow\rangle_K | +1, B, \downarrow\rangle_{K'}$. The effective gyromagnetic ratios obtained from the slopes, $g_{\perp} = 2.1 \pm 0.3$, $g_{||} = 2.4 \pm 0.1$ for Δ_2 , and $g_{||} = 2.5 \pm 0.3$ for Δ_{-2} , are close to the bare value, $g_0 = 2$, suggesting that the field dependence is controlled by spin response.

. Turning to the field dependence of Δ_3 in Figure 4b, we find that it increases linearly with in-plane field, with a slope corresponding to $g_{||} = 1.5 \pm 0.2$ and a finite field intercept, $B_0 = 1.1 \pm 0.1$ T. These results suggests that the correlated state emerging at $n/n_0 = 3$ for $B_{||} > 2.5$ T is a spin polarized insulator (Fig .4b bottom panel), consistent with the measured $C = 1$ Chern number, and with the theoretically predicted stripe ferromagnetic insulator phase.³¹

Surprises at 3.5 moiré filling

In Figure 4c,d and Extended Data Figure 11 we show the temperature and in-plane field dependence of the longitudinal resistance peak at $n/n_0 \sim 3.5$ which accompanies the VHS at $n/n_0 \sim 3.5$. Remarkably, as shown in the inset of Figure 4d for $B = 0$, the peak at $n/n_0 \sim 3.5$ increases with temperature, and reaches a maximum at $T \sim 9$ K. This suggests the emergence of an unusual insulating state at higher temperatures akin to the Pomeranchuk effect in He_3 , where a fluctuating internal flavor degree of freedom produces an entropically ordered state³². A

similar effect is also seen on the $s = \pm 1$ branch (Fig. 1b and Extended Data Figure 11a), consistent with recent reports.³³ The evolution of this peak with magnetic field suggests the emergence of a gap at higher fields resulting in the formation of a new sub-band in the fractionally filled moiré cell. This could either reflect a field-induced broken symmetry that halves the area of the moiré cell at this filling, or alternatively a fractional Chern insulator, but resolving this question is left to future work.

Summary

The results reported here demonstrate the creation of sub-bands with non-trivial topology characterized by finite Chern numbers $C = 3, \mp 2, \mp 1$ on the $s = -1, \pm 2, \pm 3$ branches respectively. For $|s| = 2, 3$, the enhanced e - e interactions, enabled by the appearance of a VHS facilitates breaking the flavor symmetry and the emergence of Chern insulators at relatively low fields. In the absence of such VHS, higher fields are required to open the correlation-induced gap on the $s = -1$, branch. Interestingly, a new VHS which is accompanied by a weakly insulating resistive state develops at $|n/n_0| = 3.5$, suggesting the emergence, at higher fields, of a correlation-induced gap and the creation of a Chern insulator at fractional moiré filling.³⁴

Author Contributions

S.W., Z.Z. and E.A. conceived and designed the experiment, carried out low-temperature transport measurement, and analyzed the data. S.W., and Z.Z. fabricated the twisted bilayer graphene devices. K.W. and T.T. synthesized the hBN crystals. S.W., Z.Z., and E.A. wrote the manuscript.

Acknowledgments

We thank M. Xie, A. H. MacDonald, M. Gershenson, S. Kivelson, A. Chubukov, G. Goldstein, G. Kotliar, T. Senthil and A. Bernevig for useful discussions and Jianpeng Liu for insightful comments and discussions. We acknowledge support from DOE-FG02-99ER45742 and from Gordon and Betty Moore Foundation GBMF9453. K.W. and T.T. acknowledge support from the Elemental Strategy Initiative MEXT-JPMXP0112101001; JSPS KAKENHI - JP20H00354 and the CREST(JPMJCR15F3), JST

References

- 1 Li, G. *et al.* Observation of Van Hove singularities in twisted graphene layers. *Nature Physics* 6, 109-113 (2010).
- 2 Suárez Morell, E., Correa, J. D., Vargas, P., Pacheco, M. & Barticevic, Z. Flat bands in slightly twisted bilayer graphene: Tight-binding calculations. *Physical Review B* 82, 121407 (2010).
- 3 Bistritzer, R. & MacDonald, A. H. Moiré bands in twisted double-layer graphene. *Proceedings of the National Academy of Sciences* 108, 12233-12237 (2011).
- 4 Luican-Mayer, A. *et al.* Screening Charged Impurities and Lifting the Orbital Degeneracy in Graphene by Populating Landau Levels. *Physical Review Letters* 112, 036804 (2014).
- 5 Wong, D. *et al.* Local spectroscopy of moiré-induced electronic structure in gate-tunable twisted bilayer graphene. *Physical Review B* 92, 155409 (2015).
- 6 Cao, Y. *et al.* Correlated insulator behaviour at half-filling in magic-angle graphene superlattices. *Nature* 556, 80-84 (2018).
- 7 Cao, Y. *et al.* Unconventional superconductivity in magic-angle graphene

- superlattices. *Nature* 556, 43-50 (2018).
- 8 Tarnopolsky, G., Kruchkov, A. J. & Vishwanath, A. Origin of Magic Angles in Twisted Bilayer Graphene. *Physical Review Letters* 122, 106405 (2019).
 - 9 Lu, X. *et al.* Superconductors, orbital magnets and correlated states in magic-angle bilayer graphene. *Nature* 574, 653-657 (2019).
 - 10 Jiang, Y. *et al.* Charge order and broken rotational symmetry in magic-angle twisted bilayer graphene. *Nature* 573, 91-95 (2019).
 - 11 Kerelsky, A. *et al.* Maximized electron interactions at the magic angle in twisted bilayer graphene. *Nature* 572, 95-100 (2019).
 - 12 Xie, Y. *et al.* Spectroscopic signatures of many-body correlations in magic-angle twisted bilayer graphene. *Nature* 572, 101-105 (2019).
 - 13 Choi, Y. *et al.* Electronic correlations in twisted bilayer graphene near the magic angle. *Nature Physics* 15, 1174-1180 (2019).
 - 14 Liu, J., Liu, J. & Dai, X. Pseudo Landau level representation of twisted bilayer graphene: Band topology and implications on the correlated insulating phase. *Physical Review B* 99, 155415 (2019).
 - 15 Song, Z. *et al.* All Magic Angles in Twisted Bilayer Graphene are Topological. *Physical Review Letters* 123, 036401 (2019).
 - 16 Kim, K. *et al.* van der Waals Heterostructures with High Accuracy Rotational Alignment. *Nano Letters* 16, 1989-1995, doi:10.1021/acs.nanolett.5b05263 (2016).
 - 17 Hofstadter, D. R. Energy levels and wave functions of Bloch electrons in rational and irrational magnetic fields. *Physical Review B* 14, 2239 (1976).
 - 18 Shi, Y. *et al.* Tunable Lifshitz Transitions and Multiband Transport in Tetralayer Graphene. *Physical Review Letters* 120, 096802 (2018).
 - 19 Badoux, S. *et al.* Change of carrier density at the pseudogap critical point of a cuprate superconductor. *Nature* 531, 210-214 (2016).
 - 20 Ashcroft, N. W. & Mermin, N. D. *Solid state physics*. (Holt, Rinehart and Winston, 1976).
 - 21 Maharaj, A. V., Esterlis, I., Zhang, Y., Ramshaw, B. J. & Kivelson, S. A. Hall number across a van Hove singularity. *Physical Review B* 96, 045132 (2017).
 - 22 Isobe, H., Yuan, Noah F. Q., Fu, Liang. Unconventional Superconductivity and Density Waves in Twisted Bilayer Graphene. *Physical Review X* 8, 041041

- (2018).
- 23 Kim, Y. *et al.* Charge Inversion and Topological Phase Transition at a Twist Angle Induced van Hove Singularity of Bilayer Graphene. *Nano Letters* 16, 5053-5059 (2016).
 - 24 Hwang, E. H. & Das Sarma, S. Impurity-scattering-induced carrier transport in twisted bilayer graphene. *Physical Review Research* 2, 013342 (2020).
 - 25 Chung, T.-F., Xu, Y. & Chen, Y. P. Transport measurements in twisted bilayer graphene: Electron-phonon coupling and Landau level crossing. *Physical Review B* 98, 035425 (2018).
 - 26 Wong, D. *et al.* Cascade of electronic transitions in magic-angle twisted bilayer graphene. *Nature* 582, 198-202, doi:10.1038/s41586-020-2339-0 (2020).
 - 27 Zondiner, U. *et al.* Cascade of phase transitions and Dirac revivals in magic-angle graphene. *Nature* 582, 203-208, doi:10.1038/s41586-020-2373-y (2020).
 - 28 Sharpe, A. L. *et al.* Emergent ferromagnetism near three-quarters filling in twisted bilayer graphene. *Science* 365, 605 (2019).
 - 29 Serlin, M. *et al.* Intrinsic quantized anomalous Hall effect in a moiré heterostructure. *Science* 367, 900 (2020).
 - 30 Cao, Y. *et al.* Strange Metal in Magic-Angle Graphene with near Planckian Dissipation. *Physical Review Letters* 124, 076801 (2020).
 - 31 Kang, J., and Vafeek, Oskar. Strong Coupling Phases of Partially Filled Twisted Bilayer Graphene Narrow Bands. *Physical Review Letters* 122, 246401 (2019).
 - 32 Richardson, R. C. The Pomeranchuk effect. *Reviews of Modern Physics* 69, 683-690, doi:10.1103/RevModPhys.69.683 (1997).
 - 33 Asaf Rozen, J. M. P., Uri Zondiner, Yuan Cao, Daniel Rodan-Legrain, Takashi Taniguchi, Kenji Watanabe, Yuval Oreg, Ady Stern, Erez Berg, Pablo Jarillo-Herrero, Shahal Ilani. Entropic evidence for a Pomeranchuk effect in magic angle graphene. *arXiv:2009.01836* (2020).
 - 34 Suen, Y. W., Engel, L. W., Santos, M. B., Shayegan, M. & Tsui, D. C. Observation of a $1/2$ fractional quantum Hall state in a double-layer electron system. *Physical Review Letters* 68, 1379-1382 (1992).

Extended Data

Methods

Sample preparations and transport measurements

The hBN/TBLG/hBN/gold stacks are prepared with the dry transfer method in a glove-box (Argon atmosphere), using a stamp consisting of polypropylene carbonate (PPC) film and polydimethylsiloxane (PDMS). Monolayer graphene, hBN flakes (30-50nm thick) were firstly exfoliated onto Si substrate capped with 285nm of thermal oxidized chlorinated SiO₂³⁵. Half of monolayer graphene is picked up by hBN on the stamp. The substrate with the remaining part of the graphene flake is rotated by $1^{\circ} \sim 1.2^{\circ}$ and picked up with the hBN/G stack. The hBN/TBLG stack is then deposited onto the bottom hBN flake that is prepared separately in advance. During the assembly of the stack the temperature is kept below 160°C. The bottom hBN flake is transferred in advance onto a gold electrode as local gate and is annealed at 250°C in Ar/H₂ for 6 hours for surface cleaning. Atomic force microscopy (AFM) and electrostatic force microscopy (EFM)³⁶ are subsequently used to identify a clean bubble-free region of the TBLG prior to depositing the electrical edge contacts (Cr/Au) for transport measurements³⁷.

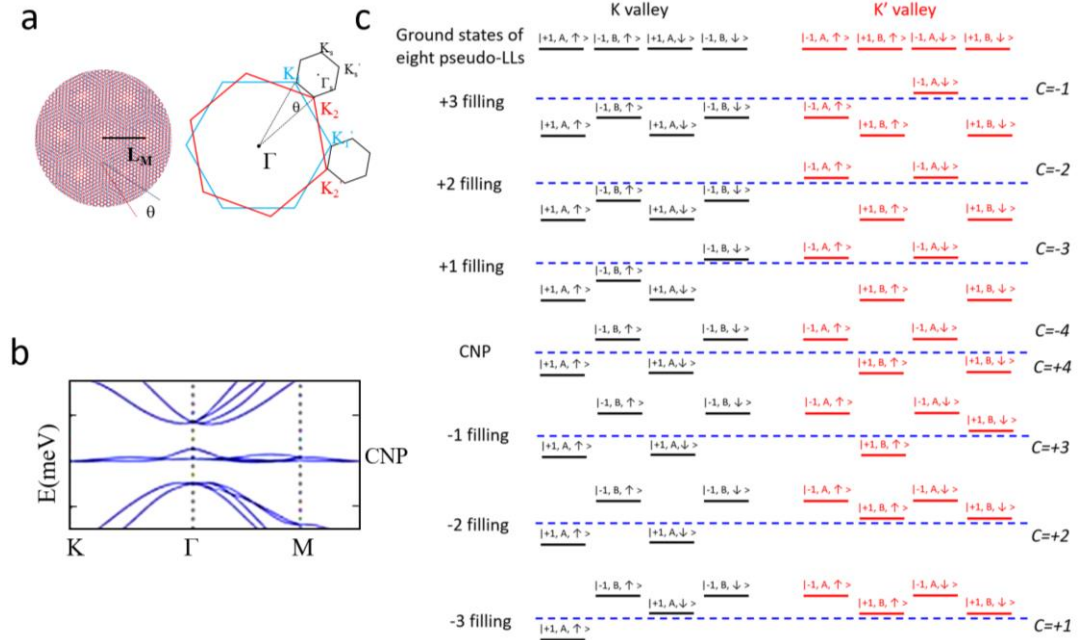
Four-terminal resistance measurements are carried out in He-3 system with a base temperature of 0.3K. The measurements are acquired with ac current excitation of 5-100nA, using standard lock-in technique at 13.7Hz as well as delta-mode of KE6221 ac current source.

Moiré pattern, Brillouin zone and flat band in MA-TBG are schematically depicted in Extended Data Figures 1a,b.

Pseudo Landau level representation of the MA-TBG flat band topology in the presence of a magnetic field

In the pseudo Landau level (pLL) picture, the flat bands in MA-TBG are mapped onto eight zeroth pLLs corresponding to Dirac fermions coupled with opposite pseudo magnetic fields ($\pm B_0$). The pLLs carry opposite Chern numbers $C = \pm 1$, and opposite sublattice polarizations A and B, in each valley. The pLLs can be described as two pairs of four-fold valley-spin degenerate flat bands carrying

positive or negative orbital magnetizations for the with $C = +1$ ($+B_0$) or $C = -1$ ($-B_0$) respectively. Applying an external magnetic field splits the $C = +1$ from the $C = -1$ Chern bands, creating a single particle gap at the CNP due to the orbital magnetic Zeeman effect. Bringing the Fermi level into these bands, the exchange part of the Coulomb interactions further lifts their degeneracy resulting in the emergence of correlated insulating states at integer band fillings, or equivalently, at integer moiré-cell fillings. Since each band carries a finite Chern number $C = \pm 1$, filling a number of these pLLs would naturally result in topological phases with nonzero total Chern number, as shown in Extended Data Figure 1c.

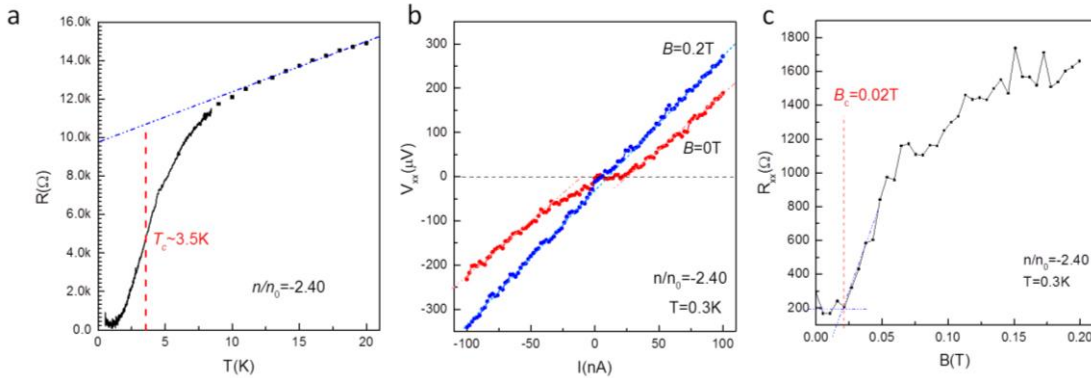


Extended Data Figure 1 | Moiré pattern, Brillouin zone, and pseudo Landau level representation of Chern insulators in MA-TBG **a**, Left panel: a moiré pattern with periodicity L_M forms by introducing a twist angle θ between the crystallographic axes for two superposed graphene layers. Right panel: The moiré mini-Brillouin zone is a hexagon constructed from the $K_s = |\vec{K} - \vec{K}'|$ where K, K' are the wave-vectors of the graphene Brillouin zone. **b**, Schematic low energy band structure of MA-TBG shows the flat bands near the CNP and the gaps separating them from the higher energy bands. **c**, Pseudo Landau level diagram of the eight states representing integer fillings of the flats band in MA-TBG. The black and red states are the states from the K_s and K'_s valleys. The indices ± 1 , A/B, and \uparrow/\downarrow represent the Chern number, sublattice polarization and spin polarization of the flat bands respectively. Note that for

$C = \pm 2$ at filling of ± 2 , only the case of valley polarized states is plotted here.

Signatures of superconductivity near $n/n_0 = -2$

Signatures of superconductivity emerge in this device below 5K. Here we focus on the moiré-filling range $n/n_0 = -2.4$. In Extended Data Figure 2a, a sharp resistance drop from $10\text{k}\Omega$ to 200Ω is observed within the temperature range 8K-0.8K. The resistance then remains nearly constant from 0.8K to 0.3K. The temperature at which the resistance drops to half its value in the normal state, defined here as the critical temperature, is $T_c \sim 3.5\text{K}$. In Extended Data Figure 2b the nonlinear current-voltage (I - V) characteristics in zero field, indicates a critical current of $\sim 12\text{nA}$. In the presence of a 0.2T magnetic field at $T = 0.3\text{K}$ Superconductivity is suppressed as shown by the linear IV. The finite resistance value ($\sim 200\Omega$) at base temperature (0.3K) and the fluctuations in the voltage fluctuations are attributed to non-ideal electrical contacts which often affect four-terminal measurements of microscopic superconducting samples as reported previously.³⁸ From Extended Data Figure 2c the critical field is estimated at $B_c \sim 0.02\text{T}$.

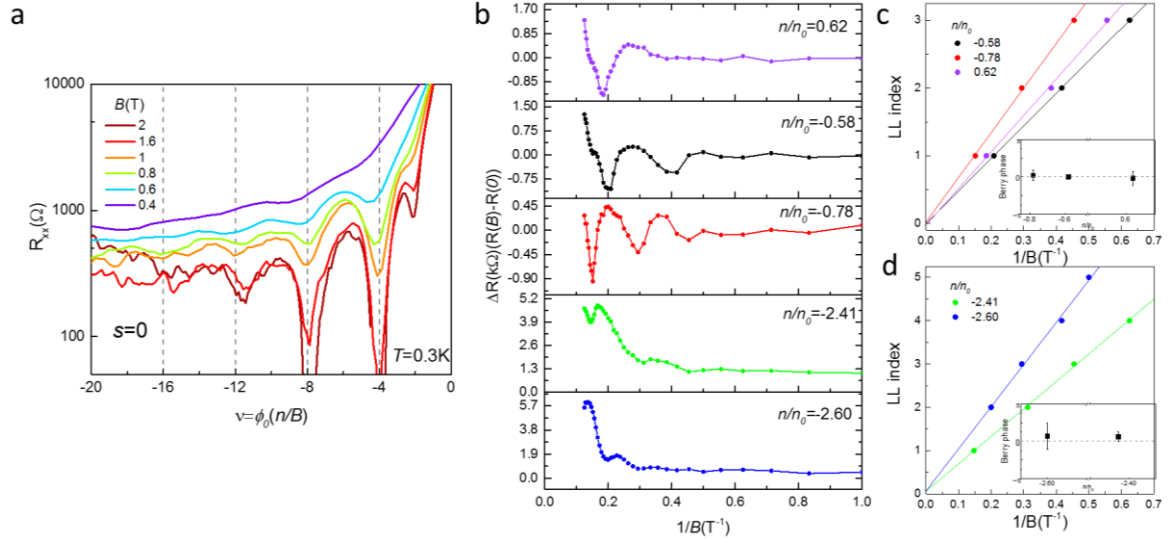


Extended Data Figure 2 | Signature of superconductivity near $n/n_0 = -2$ **a**, $R(T)$ at $n/n_0 = -2.4$. The critical temperature, $T_c = 3.5\text{K}$ is marked. The driving current is 10nA . **b**, Comparison of I - V curves at $n/n_0 = -2.4$ at zero and finite magnetic field shows suppression of critical current from 12nA down to zero. **c**, $R(B)$ curve measured with a 10nA current, indicates a critical field of $B_c \sim 0.02\text{T}$.

Shubnikov-de Haas oscillations and Berry phase.

The Landau sequence at very low field ($B = 0.4\text{T}$) exhibits 4-fold degeneracy, $\nu =$

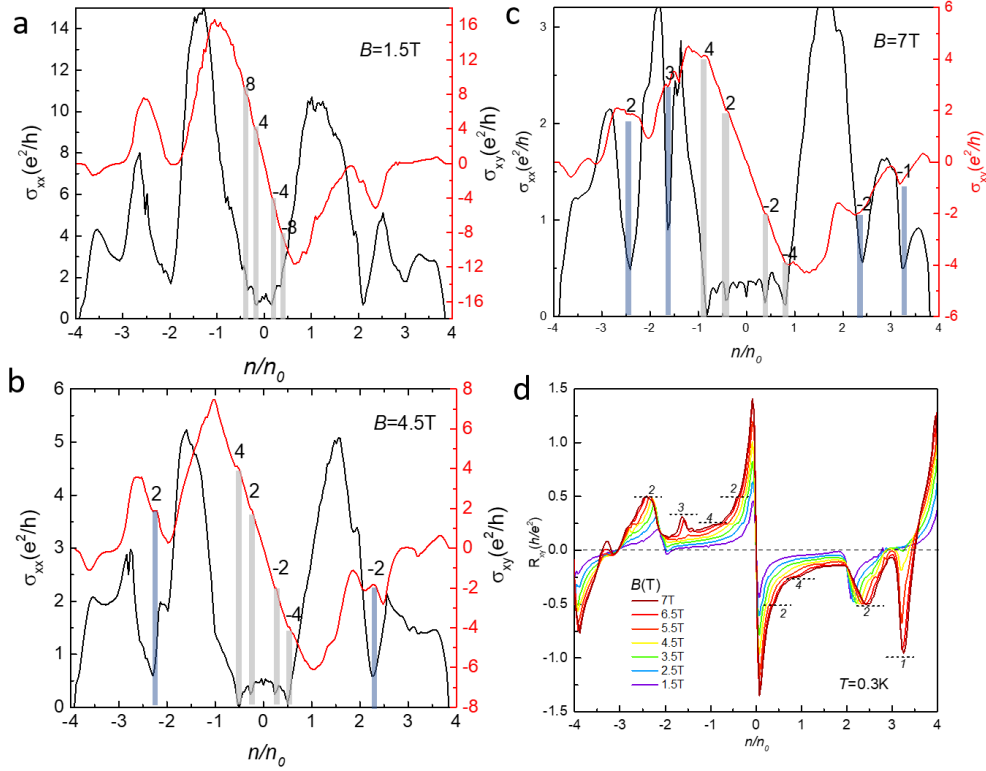
$-4, -8, -12 \dots$ as shown in Extended Data Figure 4a. The Berry phase on the $s = 0$ and $s = 2$ Landau fan branches was determined from Shubnikov-de Haas oscillations by plotting in Extended Data Figure 3c the inverse magnetic field ($1/B$) value at which the resistance minima, $\Delta R(B) = R(B) - R(0)$ obtained from Extended Data Figure 3b, occur as a function of Landau level index (LL index). Multiplying the LL index intercept of the curves in Extended Data Figure 3c,d by 2π , gives the Berry phase for each branch, which is zero in both cases. This is contrary to the zero-field non-interacting band structure calculations that find Dirac cones at the CNP³, indicating that correlation induced gaps appear already at low fields ~ 0.6 T. These results are testimony to the important role of interactions in this system, as well as to the high quality of the sample.



Extended Data Figure 3 | Berry phase obtained from Shubnikov-de Haas oscillations .

a, R_{xx} as a function of Landau filling $\nu = \phi_0(n/B)$ on the hole-side of the $s = 0$ branch at very low field ($B = 0.4 \sim 2$ T). **b**, Shubnikov-de Haas oscillations near CNP and $n/n_0 = -2$. **c-d**, $1/B$ -field location of Shubnikov-de Haas minima versus the Landau level index (LL index). The intercept of linear fits to the data points with the LL index axis multiplied by 2π gives the Berry phase. Insets: calculated Berry phase for both branches is zero

Evolution of quantum Hall plateaus in a magnetic field



Extended Data Figure 4 | Quantum Hall plateaus. **a**, $\sigma_{xy}(n/n_0)$ at 1.5T displays quantum Hall plateaus, $\sigma_{xy} = \nu \frac{e^2}{h}$, and concomitant minima in $\sigma_{xx}(n/n_0)$ (gray bars) near the CNP. The Chern number sequence $\nu = \pm 4, \pm 8$ indicates the 4-fold degeneracy. **b-c**, Same as panel (a) at 4.5T and 7T shows a new sequence with $\nu = \pm 2, \pm 4$ and concomitant minima, indicating that either spin or valley degeneracy is lifted by the field. **c, d**, Filling $R_{xy}(B)$ shows the emergence of Chern insulators in the higher order branches. All data are taken at $T = 0.3K$.

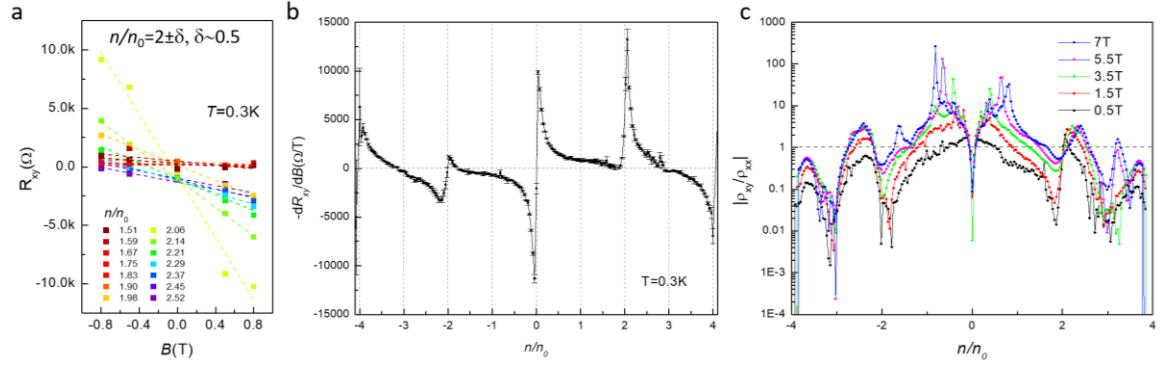
Calculating the Hall density from the Hall resistance measurements.

The Hall density, $n_H = -B/(eR_{xy})$ is calculated using the slope dR_{xy}/dB of obtained from a linear fit of the measured $R_{xy}(B)$ curves at fixed n/n_0 , as shown in Extended Data Figure 5a,b.

Estimating, $\omega_c \tau$,

The expression for the logarithmic divergence of n_H near a VHS is valid in the low-field limit²¹ $\omega_c \tau \ll 1$ where $\omega_c = \frac{eB}{m}$ is the cyclotron frequency and τ the scattering time. To ensure the validity of the fit in the main text we estimated the value of $\omega_c \tau$ as a function of density and field. Within the Drude model, $\rho_{xx} =$

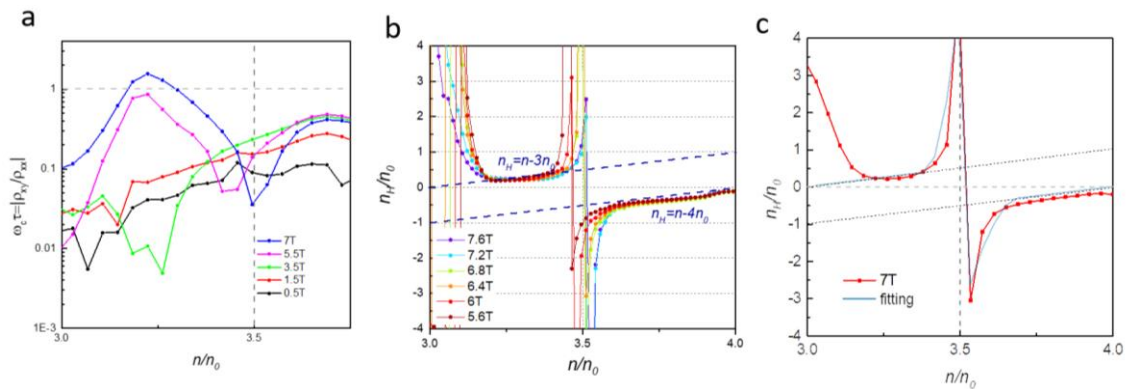
$\frac{m}{ne^2\tau}$, $\rho_{xy} = \frac{B}{ne}$, we estimate $\omega_c\tau = |\rho_{xy}/\rho_{xx}|$ shown in Extended Data Figure 5c. Clearly all the data taken near the putative VHSs is in the low field limit.



Extended Data Figure 5 | Calculating n_H and estimating $\omega_c\tau$ **a**, Linear fits of $R_{xy}(B)$ at fixed moiré fillings, n/n_0 , as indicated in the legend. **b**, Filling dependence of dR_{xy}/dB obtained by fitting $R_{xy}(B)$ curves as illustrated in panel (a). **c**, $|\rho_{xy}/\rho_{xx}| = \omega_c\tau$ as a function of n/n_0 at several fields as marked.

Divergent Hall density and the VHS point near $n/n_0 = 3.5$ in high fields

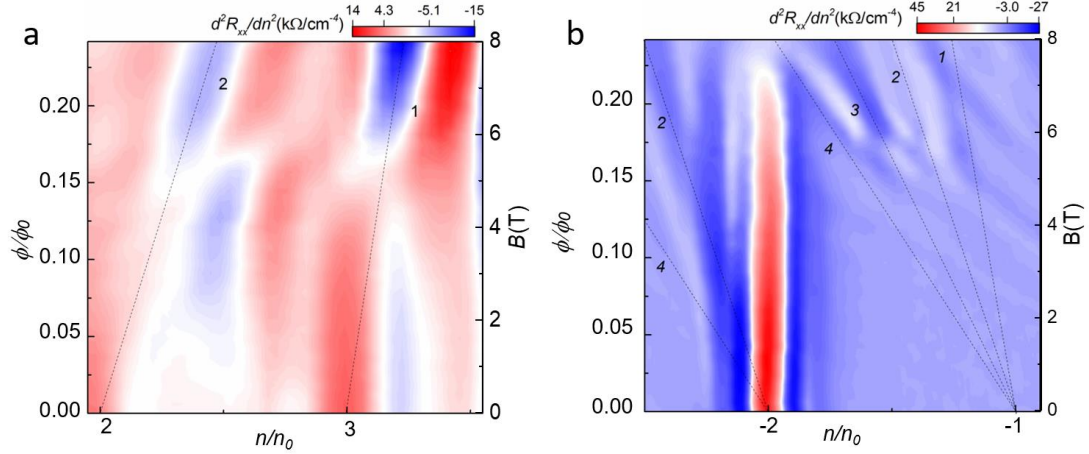
With the gap opening at $n/n_0 = 3$, we observe a divergent dependence of n_H on carrier density at $n/n_0 = 3.5$. Based on the estimate of $\omega_c\tau \ll 1$ around $n/n_0 = 3.5$ (Extended Data Figure 6a), the expression for the logarithmic divergence of VHS in the low-field limit, $n_H \approx \alpha + \beta|n - n_c| \ln|(n - n_c)/n_0|$ described in the main text was used in fitting the density dependence of n_H in this regime, as shown in Extended Data Figure 6c.



Extended Data Figure 6 | Divergent Hall density and VHS near $n/n_0 = 3.5$ **a**, $\omega_c\tau$ around $n/n_0 = 3.5$ obtained from $|\rho_{xy}/\rho_{xx}|$ at several B -fields shows that the low field limit $\omega_c\tau \ll 1$ is valid in this regime. **b**, Evolution of Hall density with field near $n/n_0 = 3.5$. Divergent n_H behavior is clearly resolved after the gap opens on the $s = 3$ branch with $n_H = n - 3n_0$. **c**, Hall density around $n/n_0 = 3.5$ fits the logarithmic

divergence (solid blue line) expected for a VHS as discussed in the main text.

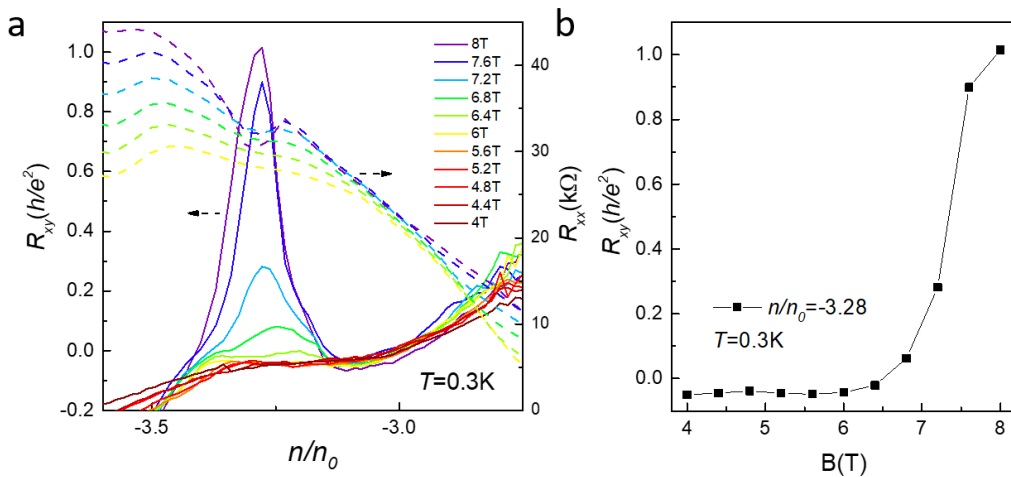
Field induced gaps and Chern insulators



Extended Data Figure 7 | Field induced insulating states at integer fillings a-b, Field and density dependence of d^2R_{xx}/dn^2 , at $T = 0.3K$ reveals the emergence of half-Landau fans on the $s = 2, 3$ branches (a) and on the $s = -1, -2$ branches (b) marked by black lines.

Quantized Hall resistance $R_{xy} = h/e^2$ in the $s = -3$ branch

In the $s = -3$ branch, quantized $R_{xy} = h/e^2$ is observed for fields above 7.2T indicating the emergence of a $C = 1$ Chern insulator as shown in Extended Data Figure 8.

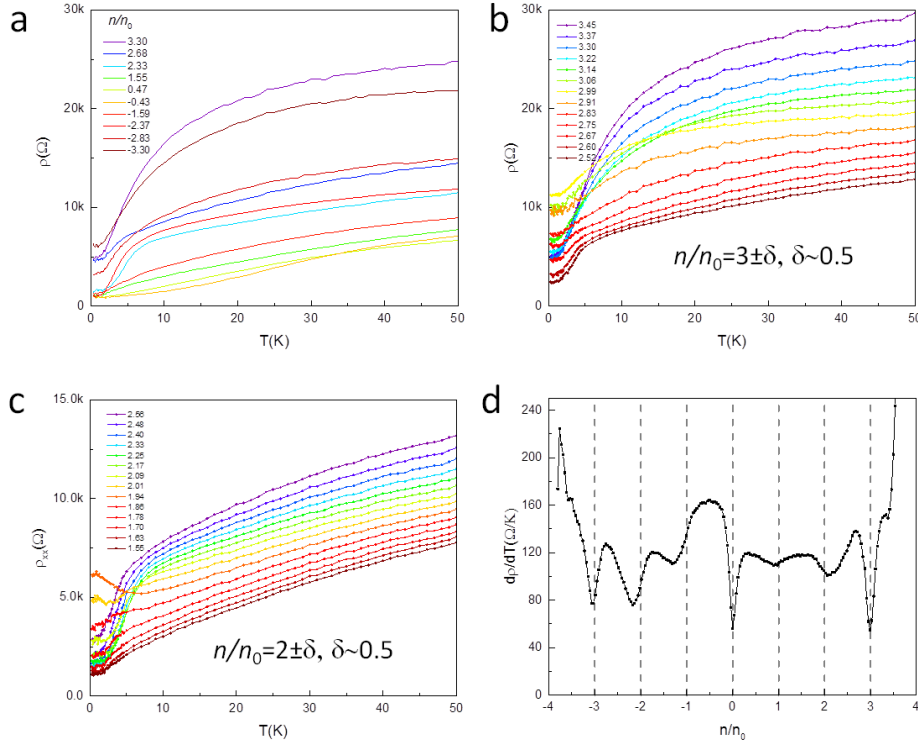


Extended Data Figure 8 | Quantized Hall resistance $R_{xy} = h/e^2$ in the $s = -3$ branch a, Hall resistance in the $s = -3$ branch, saturates at a quantized value, $R_{xy} = h/e^2$ indicating the emergence of a $C = 1$ Chern insulator. The corresponding R_{xx} curves are

shown in dashed lines. **b**, R_{xy} at fixed carrier density ($n = -3.28n_0$) as a function of magnetic field shows the onset of the emergent Chern insulator at ~ 6.5 T.

Longitudinal resistivity and its dependence on temperature and moiré filling.

The longitudinal resistivity displays linear-in temperature dependence at all moiré fillings above ~ 5 K (Extended Data Figure 9 (a-c)). The temperature derivative in the filling range $0.5 < |n/n_0| < 3.5$, is $d\rho/dT \approx 120 \pm 20(\Omega/K)$, which is comparable with the values reported by other groups.³⁰ This contribution, which is still poorly understood, has been attributed to electron-phonon interactions as well as to strange metal behavior³⁰.



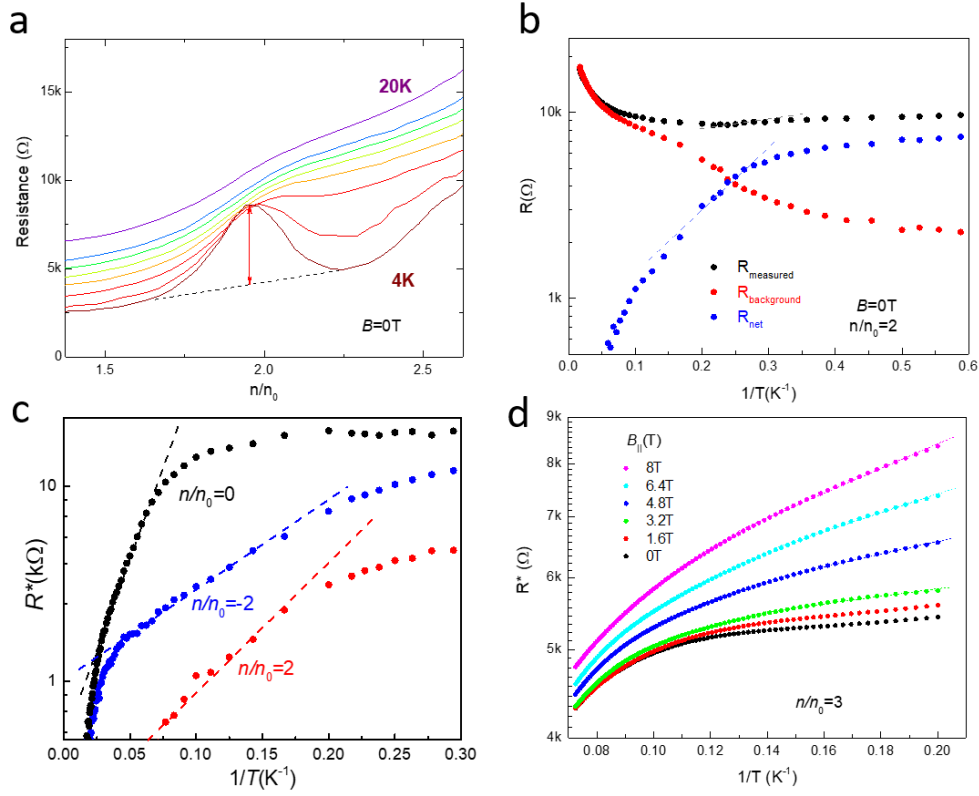
Extended Data Figure 9| Temperature and filling dependence of longitudinal resistivity. **a-c**, $\rho(T)$ curves at selected fillings. **d**, $d\rho/dT$ extracted in the linear-temperature-resistivity regions in (a-c).

Subtraction of the linear-temperature-resistivity background for the estimation of thermal activation gaps Δ_a at integer fillings

It is noted that spectroscopic gaps (e.g. at $|n/n_0| = 2$) obtained from local measurements such as STS or electronic compressibility, 7.5meV;¹¹ 4-8meV;¹³

3.9meV;³⁹ are larger than thermally activated gaps obtained from in transport, 0.31meV;⁶ 1.5meV;³⁸ 0.37meV.⁹ Such discrepancies are expected when comparing local to global probe measurements, because in the presence of gap inhomogeneity the latter are necessarily dominated by the smallest gaps.³⁹

In MA-TBG, linear T-resistivity behavior is unique and prominent thus playing a crucial role in carrier resistivity. As shown in Extended Data Figure 9, the longitudinal resistance has a linear in temperature- background that is observed at all temperatures and fillings. It is found that with decreasing temperature from 60K, even though the overall resistivity decreases linearly, the resistive humps at integer fillings start showing up which is consistent with previous reports.^{6,9} This indicates the coexistence of the T-linear behavior and onset of the correlation gap. At high temperature, phonon-scattered (thermally excited) carriers would short out the correlation gap. In order to access the thermally activated part of the resistivity, R^* , we subtract the linear in T background. The thermal activation gap, Δ , is estimated by fitting to the Arrhenius dependence, $R^* \sim \exp(-\Delta/2k_B T)$, in the temperature range 7K-15K, where k_B is Boltzmann's constant. Extended Data Figure 10a, 10b shows the results at $n/n_0 = 2$ with and without background subtraction where the value of the calculated gap is $\Delta_2 = 2.5\text{meV}$ and 0.1meV, respectively. The value obtained after background subtraction, 2.5meV, matches the temperature range where the resistance peak starts showing up, and is comparable to the energy scale of the spectroscopic gaps. In addition, the opening of the correlation gap at $|n/n_0| = 3$ with increasing magnetic field is also supported by the Hall density measurements. The linear Zeeman splitting relation is consistent with the spin response of the correlated states at integer fillings.

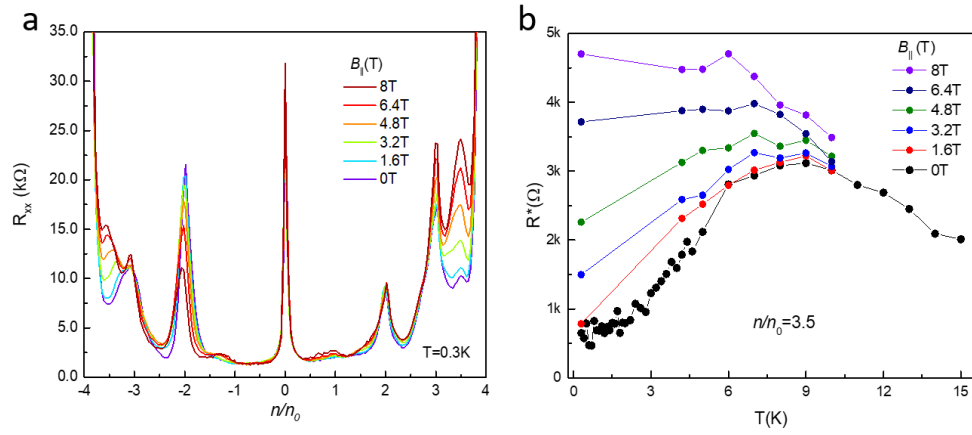


Extended Data Figure 10| Thermal activation gaps at integer fillings and in finite magnetic fields **a**, Evolution of the resistance peak around $n/n_0 = 2$ with temperature measured at $B = 0\text{T}$. The subtracted background is marked as dashed line. The net resistance (R^*) is marked by a red line with arrows. **b**, Temperature dependence of resistance at $n/n_0 = 2$ with and without subtraction of the background. **c**, Arrhenius fits of the temperature dependence of R^* are used to calculate the thermal activation gaps at integer fillings at $B = 0\text{T}$: $\Delta_0 = 7.38 \pm 0.08\text{meV}$, $\Delta_2 = 2.5 \pm 0.15\text{meV}$, and $\Delta_{-2} = 1.7 \pm 0.15\text{meV}$, for $n/n_0 = 0, 2, -2$ moiré fillings, respectively. The deviation of R^* at low temperatures from the exponential divergence expected for activated transport is attributed to variable range hopping⁴⁰, which is most pronounced at $n/n_0 = 0$ where the carrier density is lowest. **d**, Evolution of temperature dependence of the net resistance, R^* , with in-plane field amplitude, $B_{||}$, at $n/n_0 = 3$.

Evolution with in-plane field amplitude of $R^*(T)$ at $n/n_0 = 3.5$;

The miniband created by the gap opening for $B > 4\text{T}$ at moiré filling $n/n_0 = 3$ leads to a divergent Hall density at moiré filling $n/n_0 = 3.5$ that reflects the emergence of a VHS, as discussed in the main text. Another signature of this VHS is the appearance of a peak in the net resistance R^* . The initially positive slope of

$R^*(T)$ at low temperatures, indicating metallic behavior, steadily decreases with increasing field, and becomes slightly insulating at 8T (Extended Data Figure 11).



Extended Data Figure 11| a, Doping dependence of resistance at varied in-plane fields at $T = 0.3K$. **b**, Evolution of $R^*(T)$ at $n/n_0 = 3.5$ with in-plane field amplitude, $B_{||}$.

References

- 35 Luican, A., Li, G. & Andrei, E. Y. Scanning tunneling microscopy and spectroscopy of graphene layers on graphite. *Solid State Communications* 149, 1151-1156, doi:<https://doi.org/10.1016/j.ssc.2009.02.059> (2009).
- 36 Altwater, M. A. *et al.* Electrostatic imaging of encapsulated graphene. *2D Materials* 6, 045034 (2019).
- 37 Wang, L. *et al.* One-Dimensional Electrical Contact to a Two-Dimensional Material. *Science* 342, 614-617 (2013).
- 38 Yankowitz, M. *et al.* Tuning superconductivity in twisted bilayer graphene. *Science* 363, 1059-1064 (2019).
- 39 Tomarken, S. L. *et al.* Electronic Compressibility of Magic-Angle Graphene Superlattices. *Physical Review Letters* 123, 046601 (2019).
- 40 Matthews, J. & Cage, M. E. Temperature Dependence of the Hall and Longitudinal Resistances in a Quantum Hall Resistance Standard. *J Res Natl Inst Stand Technol* 110, 497-510 (2005).